Journal of
Materials Chemistry A

ROYAL SOCIETY
OF CHEMISTRY

PAPER

View Article Online
View Journal | View Issue

Check for updates

Cite this: J. Mater. Chem. A, 2025, 13, 20812

Unveiling the crucial morphological effect of non-conducting polymer binders on inorganic-rich hybrid electrolytes†

Natalia Stankiewicz,[a] Leon Focks,[bc] Mengyang Cui,[c] Mercedes Fernandez,[d] Evgenii Modin,[e] Amaia Iturrospe,[f] Oier Pajuelo-Corral,[a] Erik Simon,[g] Arantxa Arbe,[f] Peter Siffalovic,[g] Gillian R. Goward,[c] Andrey Chuvilin[e] and Irune Villaluenga *[ah]

The limited fundamental knowledge about polymer binder selection in inorganic-rich hybrid electrolytes (HSEs) hinders their optimization and translation to an industrial scale. Herein, we investigate, for the first time, the crucial morphological effect of non-conducting polymer binders in HSEs based on a halide electrolyte (Li_3InCl_6). We compared the effect of the ordered nanostructured styrene–ethylene–butylene–styrene (SEBS) block copolymer and disordered polyisobutylene (PIB) homopolymer binders. This work was aimed at understanding ionic conduction transport across halide-based inorganic-rich HSEs with different polymer morphologies to optimize their design. We investigated ionic conductivity *via* EIS and Li^+ diffusion using ^7Li PFG-NMR, and the obtained results were supported by 3D reconstruction from cryo-plasma FIB-SEM images, which were further correlated with rheology measurements. PIB HSE presented higher transport properties than SEBS HSE with higher ionic conductivity (0.39×10^{-4} and 0.23×10^{-4} S cm^{-1} at 30 °C, respectively) and ^7Li diffusion (6.3×10^{-13} and 4.3×10^{-13} m^2 s^{-1} at 30 °C, respectively) owing to a less tortuous percolated inorganic network observed *via* the 3D reconstruction of cryo-plasma FIB-SEM images. Moreover, rheology measurements indicated that HSEs composed of ordered block copolymers should be processed in the disordered state ($T > T_{ODT}$) (in which the ordered microdomains disappear), reaching the terminal flow zone as disordered homopolymers to improve the percolated inorganic network and thereby achieving high transport properties in HSEs. Finally, Li plating/stripping demonstrated a more stable electrochemical performance of PIB HSE and higher critical current density (400 μA cm^{-2}) compared with SEBS HSE (25 μA cm^{-2}), which was in good agreement with the obtained transport and morphological properties.

Received 6th February 2025
Accepted 20th May 2025

DOI: 10.1039/d5ta00979k

rsc.li/materials-a

Introduction

To overcome the safety concerns associated with lithium-ion technology, flammable liquid electrolytes are to be replaced with solid-state electrolytes in all-solid-state batteries (ASSBs). Pursuing this goal is expected to improve the energy density of batteries while prolonging their cycling stability and increasing the working voltage. Consequently, the researchers are working towards developing new solid-state inorganic materials to be applied as electrolytes, including oxides, sulfides and halides, owing to their excellent transport properties.[1] These materials are not only nonflammable but also provide improved durability, energy density, stability and a wide electrochemical window. However, they still possess a variety of features, for instance, brittleness and obligatory processing at high pressures (hundreds of MPa), which restrict their practical application in the current technology used in industrial calendaring.[2,3]

---

[a] POLYMAT, Department of Applied Chemistry, Faculty of Chemistry, University of the Basque Country UPV/EHU, Paseo Manuel de Lardizábal 3, 20018 Donostia-San Sebastián, Spain. E-mail: irune.villaluenga@ehu.eus

[b] Institute of Physical Chemistry, University of Münster, Correnstrasse 28, D-48149 Münster, Germany

[c] Department of Chemistry & Chemical Biology, McMaster University, Hamilton, Ontario, L8S 4L8, Canada

[d] POLYMAT, University of the Basque Country UPV/EHU, Joxe Mari Korta Center, Avda. Tolosa, 72, 20018 Donostia-San Sebastian, Spain

[e] CIC nanoGUNE BRTA, Tolosa Hiribidea, 76, 20018 Donostia-San Sebastián, 20012 Basque Country, Spain

[f] Centro de Física de Materiales (CSIC-UPV/EHU) – Materials Physics Center (MPC), Manuel Lardizabal Ibilbidea 5, 20018 Donostia-San Sebastián, Spain

[g] Centre for Advanced Materials Application (CEMEA), Slovak Academy of Sciences, Dúbravská cesta 9, Bratislava 84511, Slovakia

[h] IKERBASQUE, Basque Foundation for Science, Plaza Euskadi 5, 48009 Bilbao, Spain

† Electronic supplementary information (ESI) available. See DOI: https://doi.org/10.1039/d5ta00979k

The combination of inorganic and flexible polymeric materials in inorganic-rich hybrid solid-state electrolytes (HSEs) offers a possibility to overcome the previously mentioned limitations of inorganic electrolytes.[4] Herein, we focus on a halide solid-state electrolyte, Li_3InCl_6 (LIC), introduced by Sun *et al.* with promising properties, including high ionic conductivity ($\sim 10^{-3}$ S cm^{-1}) at room temperature (RT), good cycling stability and wide electrochemical window. It is also reported to be easily recovered by heating, which is beneficial from a recyclability perspective.[5,6] One of the key factors in developing an inorganic-rich hybrid electrolyte is understanding its electrochemical performance in terms of lithium-ion transport at the atomic, micro and mesoscopic scales. The movement of lithium ions is affected not only by inorganic grains but also by grain boundaries, voids between the particles, and inorganic grain-polymer boundaries.[7] Therefore, the appropriate selection of a polymer binder that is compatible with the inorganic electrolyte of choice is crucial to achieve an HSE with optimum properties (mechanical and electrochemical).[8] The application of polymer materials as binders mainly depends on their structure/morphology and chemical polarity. The chemical polarity of the polymers in inorganic-rich HSEs has been extensively studied, concluding that non-polar (non-conducting) polymers are the best candidates because they prevent any side reactions that might occur in the HSE system and do not create competitive pathways for ionic transport, which deteriorate the final properties when applied in a battery.[9] Moreover, they serve to avoid cracks, providing sufficient flexibility to enable the processing of hybrids in current battery manufacturing lines.[10] Among the typical polymer binders that are used at the industrial scale, rubber-based materials, including poly(styrene–butadiene–styrene) (SBS), styrene–ethylene–butylene–styrene (SEBS) or polyisobutylene (PIB), are promising because of their excellent flexibility and electrochemical stability as investigated by Montes *et al.*[11] Lee *et al.* investigated the polarity influence of non-conducting polymer binders (polybutadiene, polyacrylonitrile and nitrile butadiene rubber (NBR)) with similar hydrocarbon polymer chains but different degrees of nitrile groups conjugated to the main backbone to investigate the impact on the $5Li_2S$–$25P_2S_5$ electrolyte. Indeed, the X-ray diffraction (XRD) results proved the instability between the inorganic and the polyacrylonitrile binder, and the best ionic conductivity was achieved for the NBR-based HSE (up to 4.2×10^{-4} S cm^{-1}).[12] Although Tan *et al.* did not observe any interactions between the dry mixtures of $Li_7P_3S_{11}$ and different polymers (PVDF-HFP, NBR, SEBS) by Raman spectroscopy and XPS analysis, their choice of electrochemical investigation with SEBS as a HSE binder was rather explained by compatibility with the solvent and the stability of the inorganic structure during slurry processing.[13] Additionally, Tron *et al.* presented a variety of homopolymers and block copolymers (NBR, HNBR, SBS, SEBS, and PIB) applied as binders, comparing the observed mechanical properties and ionic conductivity values of Li_6PS_5Cl-based HSEs. The preparation method, involving cold-pressing or slurry casting, provided the HSEs with similar ionic conductivity for each binder, proposing the application of different polymer mixtures as HSE binders to achieve a balance of fair ionic conductivities and good mechanical properties.[14] However, the polymer morphology effect has never been studied, making the selection of a non-conducting polymer in inorganic-rich HSE a trial-and-error approach, where different inorganic materials are combined with a variety of non-conducting polymers to achieve the highest ionic conductivity values. Therefore, it is evident that a deep understanding of the influence of non-conducting polymer morphology on transport properties is needed to optimize the design of inorganic-rich HSEs efficiently.

In this work, we investigate, for the first time, the morphological effect of non-conducting rubbery polymer binders on the transport properties in hybrid halide-based (Li_3InCl_6) solid electrolytes with a high inorganic content (58 vol%) to optimize the HSE design. The comparison between two polymers, ordered nanostructured block copolymer SEBS and disordered homopolymer PIB, provides new insights into the final transport properties of flexible and self-standing thin membranes (30 μm). We compare the ionic conductivity and ^7Li diffusion using EIS and PFG-NMR, respectively. The results obtained are then supported by 3D reconstruction images from cryo-plasma FIB-SEM. The ionic transport and structure of the materials is correlated with rheological properties. Moreover, the limiting current measurements summarize the influence of the different polymer structures of HSEs studied in this work. In the rapidly growing electric vehicle market, we believe our results will decipher the effect of non-conducting polymers on the transport properties of halide-based HSEs and pave the way for developing optimized HSEs in response to the remaining challenges in all-solid-state lithium-metal battery production lines.

Experimental section

Materials preparation

First, the Li_3InCl_6 inorganic electrolyte (LIC) was synthesized by the water-mediated method. Lithium chloride (LiCl; 99.9%, ultradry; Alfa Aesar) and indium chloride ($InCl_3$; 99.999%, anhydrous; Alfa Aesar) were weighed inside the glovebox in a stoichiometric ratio (3 : 1) and dissolved in deionized water, which was subsequently evaporated at 200 °C for 5 h under vacuum, as described in detail previously in our previous work.[15] The obtained LIC was ground in a mortar before further use and exhibited an ionic conductivity of 0.23×10^{-3} S cm^{-1} at RT and 150 MPa. The preparation of hybrid solid-state electrolytes (HSEs) involved overnight mixing of the LIC dispersion in toluene (anhydrous, Scharlab) (1 g mL^{-1}) with 15 wt% styrene–ethylene–butylene–styrene (SEBS; $M_w = 118\,000$ g mol^{-1}, 29 : 71 mole ratio styrene : rubber; Sigma-Aldrich) or 5 wt% polyisobutylene (PIB; $M_w = 1\,000\,000$ g mol^{-1}; Sigma-Aldrich) solutions in toluene, casting on a Teflon Petri Dish and drying overnight at room temperature under vacuum. The amount of LIC was 80 wt% (58 vol%), and the amount of polymer was 20 wt% (42 vol%). Finally, the optimized last step involved hot pressing of the dried membranes at 200 °C or 180 °C for 30 min at 150 MPa for SEBS- or PIB-based HSE, respectively.

Material characterization

X-ray diffraction (XRD), Bruker D8 ADVANCE X-ray diffractometer, λCu-K$_{\alpha 1}$ = 1.5418 Å radiation in the scattering angle 2θ range 10–80° with a step width of 0.05°, was used to examine the crystallinity of the inorganic material. The samples were placed in an XRD holder, covered with a Kapton film inside the glovebox and transferred to the XRD equipment. The data were collected under vacuum overnight for improved XRD spectra quality. As shown in Fig. 2 and S1,† the inorganic Li_3InCl_6 phase contains its hydrated counterpart ($Li_3InCl_6 \cdot xH_2O$) due to sample transportation issues in the XRD holder from the glovebox to the XRD equipment; thus, the hydrated phase was included in the refinement in Fig. S1,† fitting well with the pattern. Two blank spaces in the refinement correspond to the sample holder contribution. The refined parameters and analysis results are presented in Tables S1 and S2.† To confirm the purity of the inorganic phase (avoiding air exposure during transfer from the glovebox to the XRD equipment), a spectrum was recorded in an air-tight capillary by synchrotron wide-angle X-ray scattering (WAXS). The WAXS pattern of the Li_3InCl_6 sample with the Rietveld refinement is shown in Fig. S2† with refined parameters and analysis results (Tables S3 and S4†), confirming the purity of the inorganic phase without the presence of $Li_3InCl_6 \cdot xH_2O$.

The polymer structure was investigated using an Avance III 300 MHz digital NMR spectrometer and deuterated chloroform ($CDCl_3$) solvent. Thermogravimetric analysis (TGA) (PerkinElmer TGA 8000) was performed from 40 to 800 °C under an N_2 atmosphere at 10 °C min^{-1}. The thermal properties were studied using differential scanning calorimetry (DSC) (PerkinElmer DSC 8000) in the range of −40 to 240 °C with a heating rate of 10 °C min^{-1} under N_2 atmosphere. The samples for DSC were placed in aluminum pans inside the glovebox using approximately 5 mg of the sample. Li diffusion in the hybrids, D(Li), was measured using ^{7}Li Pulsed-Field Gradient Nuclear Magnetic Resonance (PFG-NMR). The samples were cut into disks of 3.5 mm diameter and placed in the home-made cell in order to conduct measurements at the desired stack pressure (from 0 to 25 MPa) by applying torque after assembling. Then, the cell was sealed with H-grease and parafilm to avoid air exposure. Gradient strength and duration were set to 2200 G cm^{-1} and 1.4 ms, respectively. The diffusion time was kept at 200 ms, except for the variable temperature experiment. During the experiments, the temperature was controlled using Bruker's VT unit equipped with BCU-II. The morphology of the electrolytes was investigated using Focused Ion Beam Scanning Electron Microscopy (FIB-SEM). The samples were packed inside the glovebox under an argon atmosphere and then transferred to the SEM vacuum chamber using the PP3010 Cryo Sample Preparation System (Quorum Technologies, UK). SEM imaging and 3D reconstruction were performed using the Amber X dual-beam instrument (Tescan, Czech Republic). First, a piece of silicon with a thickness of 15 μm was placed on top of the sample to minimize curtaining artefacts during milling. The cross-section of the region of interest was roughly polished away from the sample's edge using a high beam current of approximately 2 μA to prepare a cross-sectional area around 500 μm wide. Subsequently, the cross-section was polished stepwise, gradually reducing the beam current. For the final serial cuts during 3D data acquisition, a beam current of 30 nA was used. To eliminate curtaining, a rocking stage was employed with rocking angles set to ±7°. Images were recorded using a low-energy backscattered electron detector (LE BSE) while the microscope operated at a beam energy of 2–3 kV and a beam current of 300 pA. Three-dimensional characterization of the samples was achieved using FIB-SEM tomography, with data collected through the Tescan FIB-SEM Tomography Advanced software. Two datasets were recorded: SEBS HSE: high-resolution dataset ~75 × 47 × 18 μm (XYZ) with a voxel size of 25 × 25 × 50 nm, which gives 3000 × 1885 × 364 voxels and PIB HSE: high-resolution dataset ~29 × 26 × 14 μm (XYZ) with a voxel size of 15 × 15 × 50 nm, which gives 1944 × 1791 × 287 voxels. Three-dimensional (3D) reconstructions and data analysis were performed using Avizo software (Thermofisher, USA). Finally, Rheometer ARES-G2 was used to investigate the structural changes in the materials. Non-destructive tests of small amplitude oscillatory shear sweeps were conducted from 0.006 to 100 rad s^{-1} at a fixed oscillation strain of 0.2% for the neat polymers and from 0.03 to 100 rad s^{-1} for HSEs. All rheological measurements for the HSEs were performed under the N_2 atmosphere and with the AtmosBag protection provided by Sigma-Aldrich. Pure polymers did not require an inert atmosphere during the measurements.

Electrochemical characterization

The total ionic conductivity was measured using electrochemical impedance spectroscopy (EIS) in the frequency range of 7 MHz to 1 Hz with a signal amplitude of 40 mV and VMP200 from Biologic. Before the measurements, the HSEs were hot pressed for 30 min at 150 MPa and a temperature of 200 °C or 180 °C (for SEBS HSE and PIB HSE, respectively) between carbon-coated aluminum current collectors with a diameter of 16 mm. The EIS measurements were recorded every 10 °C increase from 30 °C to 90 °C. Ionic conductivity σ [S cm^{-1}] was calculated by the equation:

$$\sigma = \frac{l}{RA}$$

where l is the membrane thickness [cm], A is the active surface area [cm^2] and R is the total resistance [Ω].

The activation energy (E_a) of the hybrids was calculated using the equation:

$$\sigma(T) = A \exp\left(-\frac{E_a}{k_B T}\right)$$

where A is the pre-exponential constant, E_a is the energy of activation calculated from the slope of the Arrhenius plot [eV], k_B is the Boltzmann constant [J K^{-1}] and T is the temperature [K].

Finally, the cycling of lithium symmetric cells was performed to evaluate the electrochemical performance of the SEBS HSE and PIB HSE hybrids. Commercial Li_6PS_5Cl (LPSCl, NEI Corporation, particle size ~1 μm) solid electrolyte was used as an interlayer, and metal lithium foil (Sigma-Aldrich) was used as the source of lithium. A custom-designed cell with a diameter of 4 mm was used for assembly. In the first step, 15 mg of LPSCl was placed inside the cell, which was lightly densified. Subsequently, the HSE was placed on the surface of LPSCl. Another 15 mg of LPSCl powder was added to cover the other side of the hybrid electrolyte. The cell was subjected to a pressure of approximately 380 MPa for 3 min to densify the powder. In the last step, a lithium foil with a diameter of 2.5 mm (surface of the lithium foil was brushed before assembling) was placed on both sides of LPSCl. Then, a pressure of 50 MPa was applied to the cell to ensure good contact between the lithium foil and the densified LPSCl. Before galvanostatic cycling of the symmetric cells, the pressure decreased to 10 MPa. Galvanostatic cycling of the symmetric cell was performed at RT on Autolab from Metrohm (type: PGSTAT302N). The cells were initially cycled at 25 μm cm^{-2} and subsequently, the current density was gradually increased to 50 μA cm^{-2}, 100 μA cm^{-2}, 200 μA cm^{-2}, 400 μA cm^{-2}, 800 μA cm^{-2} and 1000 μA cm^{-2}, with four platings/strippings performed at each current density.

Results and discussion

In the pursuit of obtaining ASSBs with increased energy density, we aimed to develop free-standing LIC-based hybrid solid-state electrolytes (HSEs) of low thickness (<50 μm) by applying two non-conducting polymers with different morphologies (ordered and disordered) as binders. We selected non-conducting polymer binders to prevent side reactions with the halide electrolyte and the formation of competitive pathways for Li-ion transport. The first polymer binder is an ordered elastomeric block copolymer combining the styrene block and ethylene/butadiene as rubbery parts.[16,17] The second binder of choice is a disordered elastomeric PIB homopolymer rubber comprising polymerized isobutylene units. The preparation of the halide-based HSEs included the synthesis of Li_3InCl_6 by water evaporation at 200 °C under vacuum. Later, the inorganic dispersion in toluene was mixed with a SEBS (15 wt%) or PIB (5 wt%) solution with the amounts calculated to achieve 80 wt% (58 vol%) of inorganic and 20 wt% (42 vol%) of polymer in a final composition. After casting the mixtures and solvent evaporation, the membranes were hot-pressed, a crucial step to create improved Li-ion pathways through a percolation network between the ion-conducting inorganic LIC particles, and additionally, eliminate the porosity that has a detrimental influence on the electrochemical performance of HSE. PIB HSE was hot-pressed at three different temperatures: 150, 180 and 200 °C at 150 MPa for 30 min in order to study the optimum conditions. The ionic conductivity was calculated to decide the optimum processing temperature for PIB HSE, and the results are shown in Fig. 1a. The ionic conductivities were 0.23×10^{-5}, 0.17×10^{-4} and 0.21×10^{-5} S cm^{-1} at 25 °C (RT) for 150, 180 and 200 °C at 150 MPa for 30 min, respectively. Thus, the optimum conditions for the hot pressing step of PIB HSE were determined to be 180 °C at 150 MPa for 30 min. For the SEBS HSE, a temperature of 200 °C at 150 MPa for 30 min was chosen to achieve the highest ionic conductivity values, as previously investigated by our group.[15] Therefore, for further comparison, we focus on the two membranes: SEBS HSE after processing at 200 °C and PIB HSE after processing at 180 °C at the same pressure (150 MPa) and time (30 min), and the schematic preparation route is depicted in Fig. 1b.

Both hybrids have similar thicknesses of 32 μm for SEBS HSE and 36 μm for PIB HSE. The preparation method for the HSEs does not affect the inorganic crystalline structure of Li_3InCl_6 (LIC), as confirmed by XRD (Fig. 2a). Both HSEs exhibit characteristic peaks at 14, 28, 29, 34 and 49°, corresponding to the Li_3InCl_6 monoclinic structure. ^{1}H-NMR was performed to verify that the polymer chemistry/nature was maintained intact after the preparation method (Fig. 2b). For SEBS HSE and SEBS, the peaks at 0.85 and 1.88 ppm correspond to the ethylene/butylene part, and 6.55 and 7.11 ppm are the signals from aromatic protons of the polystyrene block. The peaks at 1.13 and 1.44 ppm for PIB HSE and PIB are associated with methyl and methylene groups, respectively. The similar integration values of the corresponding chemical shift peaks for each binder structure in the neat polymers and their HSE analogues confirm the unaltered chemical structures of SEBS and PIB in HSEs.

Subsequently, the thermal properties of the HSEs were studied. Firstly, the thermal stability of the obtained HSEs was investigated by TGA. This enables evaluation of the degradation temperature and the safety of the materials when applied as a component of ASSB. Both hybrids are stable up to 367 °C for SEBS HSE and 306 °C PIB HSE, as shown in Fig. 3a, providing battery safety with excellent thermal stability. Additionally, DSC measurements were conducted to observe non-phase transitions of the inorganic and polymer parts of the materials. There were no thermal events observed for both hybrids and their neat polymer binder references during the DSC scans, except for a small heat flow change (50–90 °C) for SEBS due to the residuary relaxation of polymer chains (Fig. 3b).[18]

For a deeper understanding of the interplay between the inorganic electrolyte and polymer binders in our hybrids, the transport properties of the hybrids were studied by EIS measurements. The typical EIS spectra and equivalent circuits for fitting the data of both HSEs are provided in Fig. 4a. The total resistance corresponding to the hybrid bulk is decoupled into two contributions. The resistance value at the intersection with the *x*-axis in the high-frequency region was assumed to be the sum of the bulk and grain boundary resistances of the inorganic LIC electrolyte ($R_{GB+bulk}$), and we attributed the second contribution at lower frequencies to the resistance between the polymer and the inorganic LIC particle (R_{int}). The resistance values were normalized by the thickness of each HSE. The $R_{GB+bulk}$ and R_{int} values at different temperatures (from 30 °C to 90 °C) are plotted in Fig. 4b and c, respectively. $R_{GB+bulk}$ decreases by 13% from 2710 ohm cm^{-1} at 30 °C to 2360 ohm cm^{-1} at 90 °C for SEBS HSE, and a decrease of 28% from 2980 ohm cm^{-1} at 30 °C to 2140 ohm cm^{-1} at 90 °C is observed for PIB HSE (Fig. 4b). The interface resistance between the inorganic particles and the polymer binder (R_{int}) presents a decrease of 63% for SEBS HSE (from 19 050 ohm cm^{-1} at 30 °C to 7060 ohm cm^{-1} at 90 °C), and of 89% for PIB HSE (from 9780 ohm cm^{-1} at 30 °C to 1120 ohm cm^{-1} at 90 °C). Therefore, R_{int} is

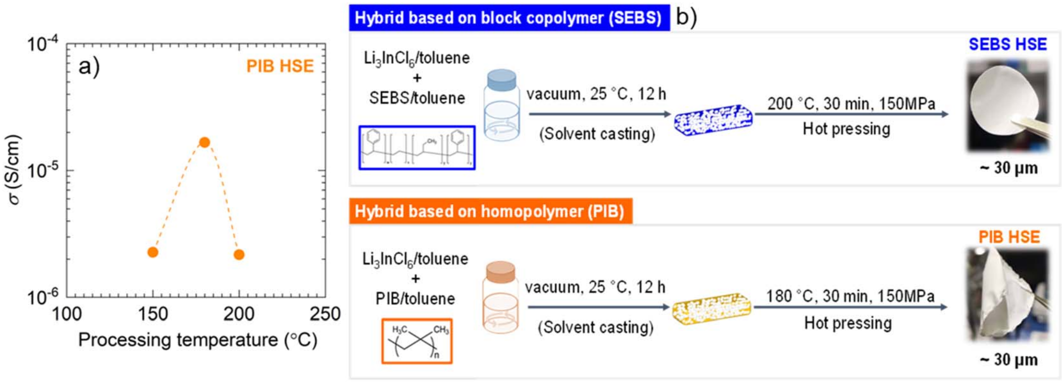

Fig. 1 (a) Ionic conductivity at 25 °C *versus* hot pressing temperatures at 150 MPa for 30 min for PIB HSE. (b) Schematic of the HSEs preparation process.

higher than $R_{\mathrm{GB+bulk}}$ in both HSEs; thus, it is evident that the ionic conductivity is dominated by the polymer–inorganic interface, with R_{int} for SEBS HSE being higher than R_{int} for PIB HSE at any temperature. Moreover, the characteristic frequency assigned to the polymer–inorganic interface varies from 560 kHz to 680 kHz for SEBS HSE and from 557 kHz to 564 kHz for PIB HSE at 30 °C and 90 °C, respectively. For a further explanation of the transport properties in the hybrids affected by temperature, we calculated the ionic conductivity and measured lithium diffusion using PFG-NMR. Ionic conductivity values from 30 °C to 90 °C for both hybrids are shown in Fig. 4d. As expected, the ionic conductivity was higher for PIB HSE (from 0.39×10^{-4} S cm^{-1} at 30 °C to 1.52×10^{-4} S cm^{-1} at 90 °C) than SEBS HSE (from 0.23×10^{-4} S cm^{-1} at 30 °C to 0.54×10^{-4} S cm^{-1} at 90 °C). As shown in Fig. 4e, the long-range ^{7}Li diffusion values were measured by PFG-NMR for both HSEs at 20 °C, being 4.2×10^{-13} and 3.7×10^{-13} m^2 s^{-1} for PIB HSE and SEBS HSE, respectively. As the temperature increases, the PIB HSE exhibits much faster ^{7}Li diffusivities than the SEBS HSE. However, the Li$^+$ dynamics measured by T_1 relaxometry (Fig. 4f) did not reveal any significant difference between the two samples throughout the entire temperature range. The Bloembergen–Purcell–Pound (BPP) relaxation theory correlates T_1 relaxation with the averaging dipolar coupling interaction resulting from the local ion hopping process,[19] whereas PFG is suited to probe long-range translational motion on the micrometer scale.[20] Therefore, the combined results from ^{7}Li relaxometry and PFG suggest that although the local Li$^+$ behavior in both the SEBS and PIB HSEs is fundamentally similar, the SEBS HSE shows a much more restricted long-range Li$^+$ mobility. This suggests a potentially poorly connected inorganic network in the SEBS HSE compared to the PIB HSE. Therefore, faster ^{7}Li diffusion was obtained for PIB HSE than SEBS HSE, which is in very good agreement with the ion conductivity results. This indicates improved particle–particle contact for PIB HSEs, and consequently, less tortuous ion-conducting channels.

The activation energy (E_a) was calculated for both HSEs using EIS measurements, following the Arrhenius equation with similar values of activation energy, 0.24 eV and 0.17 eV for PIB HSE and SEBS HSE, respectively. These values are in very good agreement with the values of E_a obtained from ^{7}Li diffusion

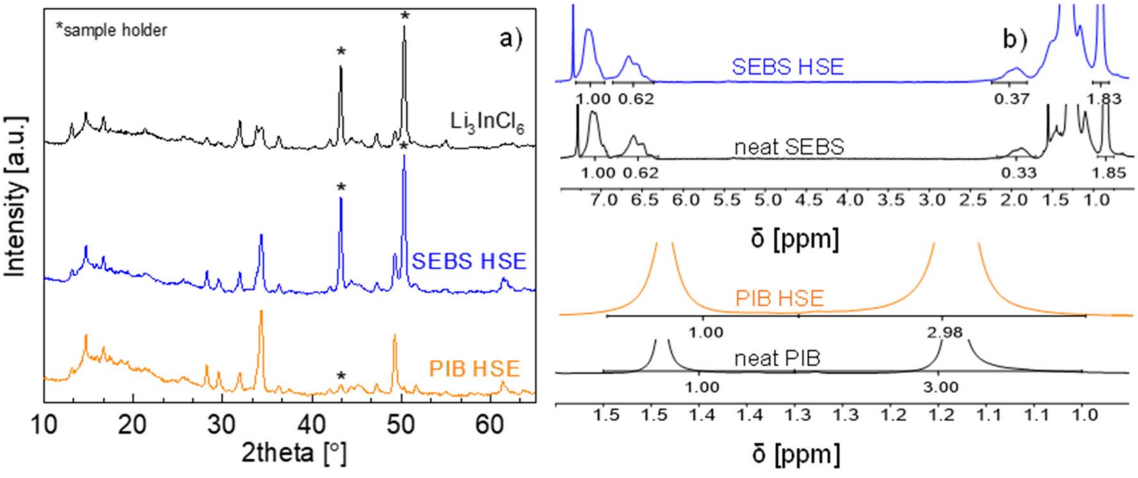

Fig. 2 (a) XRD pattern of Li_3InCl_6, SEBS HSE and PIB HSE and (b) ^{1}H-NMR spectra comparison between SEBS HSE, PIB HSE and the corresponding neat polymer binders (SEBS and PIB).

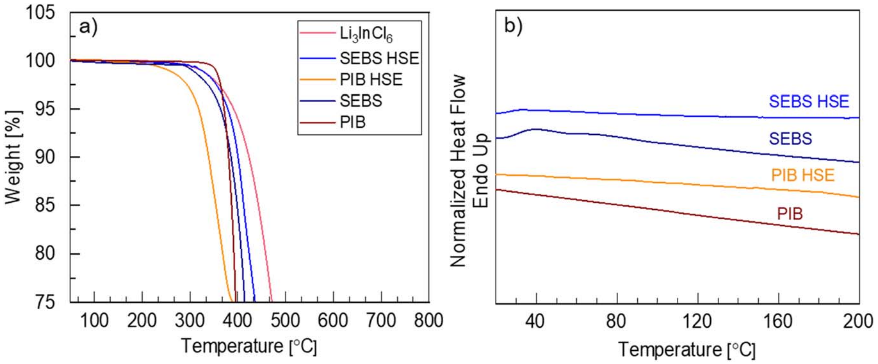

Fig. 3 (a) Thermograms of Li_3InCl_6, SEBS, PIB, SEBS HSE and PIB HSE. (b) DSC curves for the second heating scan for SEBS, PIB, SEBS HSE and PIB HSE.

measurements by PFG-NMR, 0.26 eV and 0.19 eV for PIB HSE and SEBS HSE, respectively. Therefore, ion transport in PIB HSE is evidently more thermally activated than in SEBS HSE.

In pursuit of atmospheric pressure operational ASSB, the influence of stack pressure on ionic conductivity values during EIS measurements was studied. The pressure effect on the ionic conductivity of the HSEs at room temperature (RT, 25 °C) was compared with that of the pure LIC to study the impact of the polymer binder. As shown in Fig. 5a, PIB HSE exhibited ionic conductivity values of 0.26×10^{-4} S cm^{-1} and 0.17×10^{-4} S cm^{-1} at 30 MPa and 150 MPa, respectively. SEBS HSE showed conductivities of 0.16×10^{-4} S cm^{-1} and $0.98 \times$

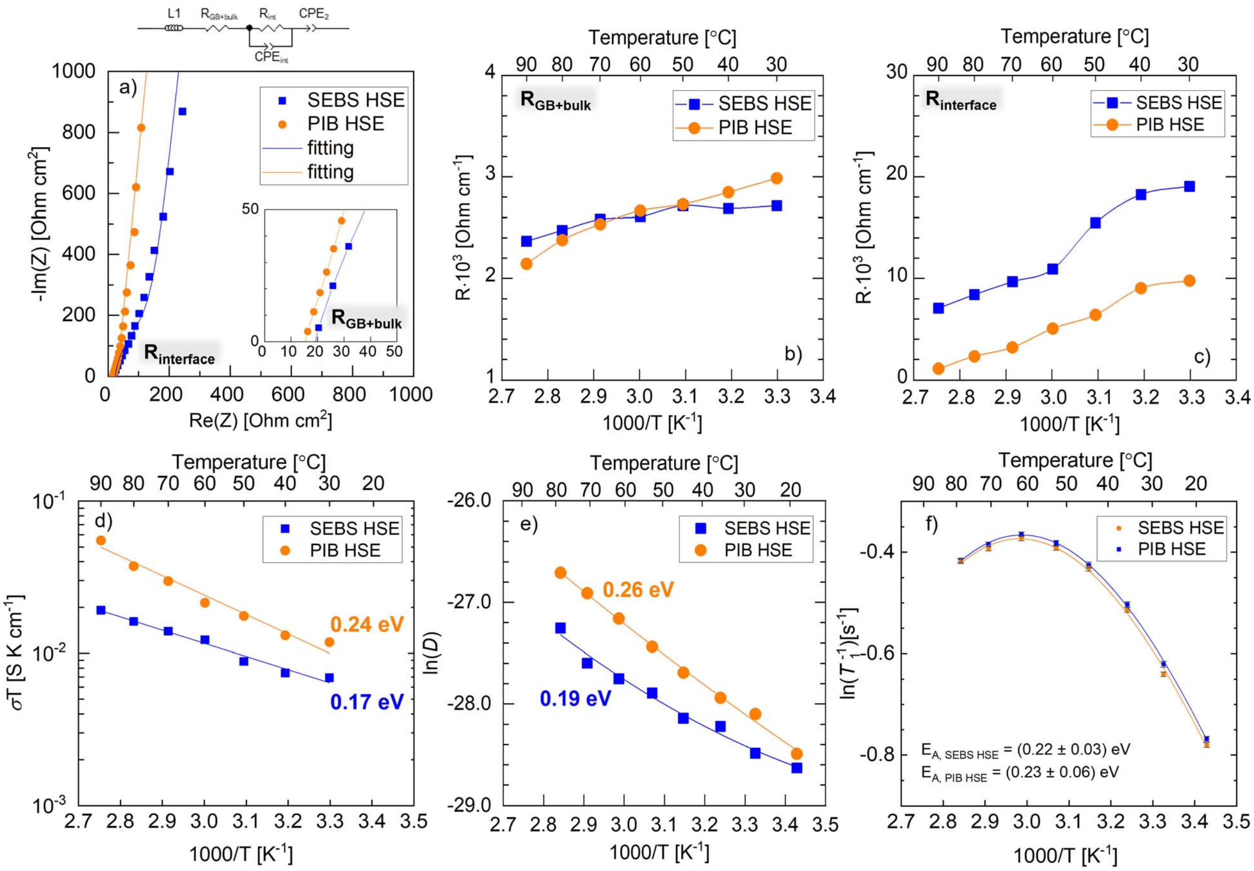

Fig. 4 (a) Exemplary Nyquist plots at 40 °C for SEBS HSE and PIB HSE of similar thicknesses, with 0–50 ohm cm^2 zoom-in in the inset, and the corresponding equivalent circuit used for the EIS spectra fittings at the top of the graph. (b) Resistance values normalized by thickness: GB + bulk resistance and (c) polymer–inorganic resistance *vs.* temperature at 150 MPa for SEBS HSE and PIB HSE. (d) σT *vs.* temperature dependence for SEBS HSE and PIB HSE at 150 MPa. (e) Temperature dependence on ln(D) for SEBS HSE and PIB HSE after processing at 150 MPa. (f) Temperature-dependent T_1 relaxometry measurements for the SEBS and PIB HSEs.

10^{-5} S cm^{-1} at 30 MPa and 150 MPa, respectively. Therefore, unlike pure LIC, a minimal pressure effect on ionic conductivity was observed for both hybrids. The inorganic LIC electrolyte exhibited conductivities of 0.11×10^{-4} S cm^{-1} and 2.28×10^{-4} S cm^{-1} at 30 MPa and 150 MPa, respectively. It is worth noting that the pristine LIC reached the ionic conductivity plateau after 110 MPa (2.11×10^{-4} S cm^{-1}), which is very similar to the ionic conductivity at 150 MPa. Therefore, the pure LIC electrolyte requires the application of high pressure in order to achieve intimate contact between the inorganic particles, in contrast to hybrids, which are almost independent of pressure after the hot-pressing step. As shown in Fig. 5b, the obtained EIS results for SEBS HSE are in very good agreement with the results of ^{7}Li diffusion from PFG-NMR measurements at pressures ranging from 0 MPa to 25 MPa. The effect of pressure on D(Li) was not observed (average $5.73 \times 10^{-13} \pm 7 \times 10^{-14}$ m^2 s^{-1} at RT for all the pressure ranges). These results have an impact from a manufacturing point of view because they can facilitate the battery assembly process and provide insights into stack pressure to be applied to already existing battery lines.[21]

To understand the higher transport properties of PIB HSEs compared to SEBS HSEs, dark-field cryo-plasma FIB-SEM was performed to study the hybrid structure by cross-section images, as shown in Fig. 6. The dark phase corresponds to the phase with lower electron density, *i.e.*, polymer binder in the hybrid, and the light phase corresponds to the inorganic LIC electrolyte. It is evident that the amount of polymer is significantly higher around the LIC particles in SEBS HSE (Fig. 6a) than in PIB HSE (Fig. 6b), which probably leads to a smaller number of connected LIC particles in SEBS HSE than in PIB HSE.

The stack images obtained from cryo-plasma FIB-SEM were used to generate 3D models of the inorganic and polymer binder regions of the HSEs to investigate the structure of the hybrids in detail.[22–24] An automatic running threshold (Avizo 8.1 software, FEI) algorithm was used to separate the inorganic and polymer HSEs components. The results are shown in Fig. 7, with the combined inorganic phase (gray) and colored polymeric phase (blue for SEBS and orange for PIB) depicted in Fig. 7a and d, respectively.

It is important to note that both hybrids do not present any porosity that could interfere with ionic transport. In fact, the vast majority of the conducting inorganic particles are connected (Fig. 7b and e) with only a small fraction of isolated LIC electrolyte for the total volume of both HSEs with 0.4% for SEBS HSE and only 0.03% for PIB HSE (Fig. 7c and f, respectively). Interestingly, the amount of those unconnected inorganic grains is 13 times higher for the HSE based on the ordered nanostructured block copolymer SEBS (Fig. 7c) compared to the disordered HSE with the homopolymer PIB binder (Fig. 7f). This is consistent with the enhanced transport properties (ionic conductivity and ^{7}Li diffusion results) for PIB HSE than SEBS HSE, as discussed in Fig. 4.

Generally, an ideal solid-state electrolyte is composed of a percolated network of clusters or particles with the lithium ions moving across the electrolyte in a straight line. However, this movement is disrupted by the presence of the non-conducting polymer binder in HSEs, introducing tortuosity to the system, affecting the percolated network, and worsening the transport properties as the ionic pathways are disturbed. Using a similar methodology to that of Duan *et al.*,[22] the inorganic LIC separated clusters and their corresponding connected mass centers were determined, as shown in Fig. 8. The colors of the clusters in Fig. 8a and c are assigned randomly. SEBS HSE presents a significantly higher amount of smaller LIC clusters (Fig. 8a) than PIB HSE (Fig. 8c), and therefore, a more tortuous percolated network, which is translated into inferior ionic transport properties in SEBS HSE. The presence of larger LIC clusters in PIB HSE decreases the tortuosity for the Li-ion pathway, reducing also the contribution of grain boundaries, which translates to facilitated ionic transport across the hybrid. The connectivity of the inorganic phase in both our hybrids was confirmed by presenting each connected mass centers of inorganic clusters, as shown in Fig. 8b and d. The images of SEBS HSE (Fig. 8b) and PIB HSE (Fig. 8d) show the percolated structure with all the inorganic clusters connected (depicted as solid lines), allowing the movement of Li-ions. The colored spheres represent the size of the LIC clusters in Fig. 8a and c, and the

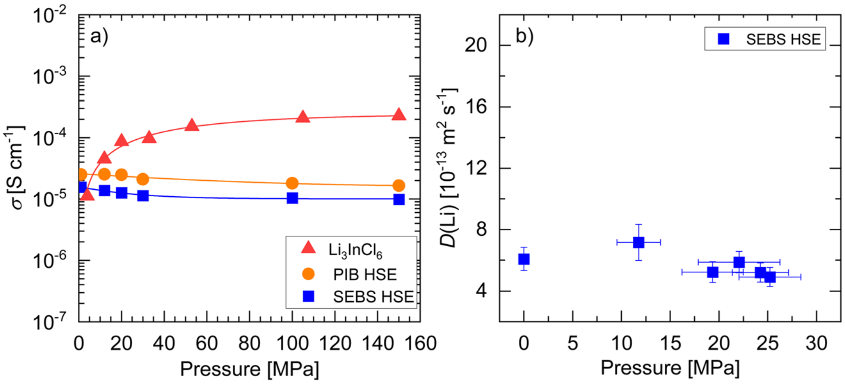

Fig. 5 (a) Ionic conductivity (σ) at 25 °C as a stack pressure function for SEBS HSE, PIB HSE and Li_3InCl_6, with solid lines to guide the eye. (b) ^{7}Li diffusion (D(Li)) *vs.* pressure at RT for SEBS HSE.

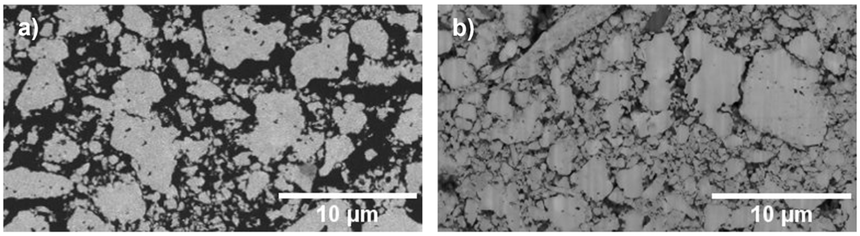

Fig. 6 Cross-sectional SEM images of (a) SEBS HSE and (b) PIB HSE.

color gradient scales correspond to the LIC clusters in SEBS HSE and PIB HSE, respectively. The connected mass centers of inorganic clusters present a bigger size for PIB HSE, with the majority typically ranging from 200 to 600 μm^3 (represented by yellow to red color in the corresponding scale bar in Fig. 8d), compared to SEBS HSE (with majority clusters with the size between 10–200 μm^3, corresponding to blue to green color as the scale bar in Fig. 8b). Overall, the 3D reconstruction images prove the different connectivity of the LIC phase in our hybrids, influencing the ionic transport. These results indicate that Li-ion transport in inorganic-rich HSEs composed of non-conducting polymers depends on the polymer morphology (ordered or disordered), which alters the sizes of inorganic clusters, and therefore, the percolated inorganic network, thereby interfering with the tortuosity of the lithium pathways in HSEs.

To clarify the polymer morphology effect on the transport properties of HSEs, conducting oscillatory shear measurements were performed on neat polymers (SEBS and PIB) and HSEs, as shown in Fig. 9. Firstly, the storage (G') and loss (G'') moduli were measured in oscillatory frequency sweep in the range of frequencies from 0.006 rad s^{-1} to 100 rad s^{-1} for neat polymer binders (SEBS and PIB at their processing temperatures (above their T_g): 200 °C and 180 °C, respectively).

The storage (G') and loss (G'') moduli (left side y-axes in Fig. 9a and b) are higher for SEBS (2.9×10^5 Pa and 1.1×10^5 Pa at 10 rad s^{-1}, respectively) than PIB (2.1×10^5 Pa and 0.6×10^5 Pa at 10 rad s^{-1}, respectively), demonstrating higher resistance to the flow of SEBS. The crossing point at low angular frequencies where G'' surpasses G' values indicates the transition from elastic solid to viscous behavior in viscoelastic materials. The viscoelastic responses of neat PIB show the

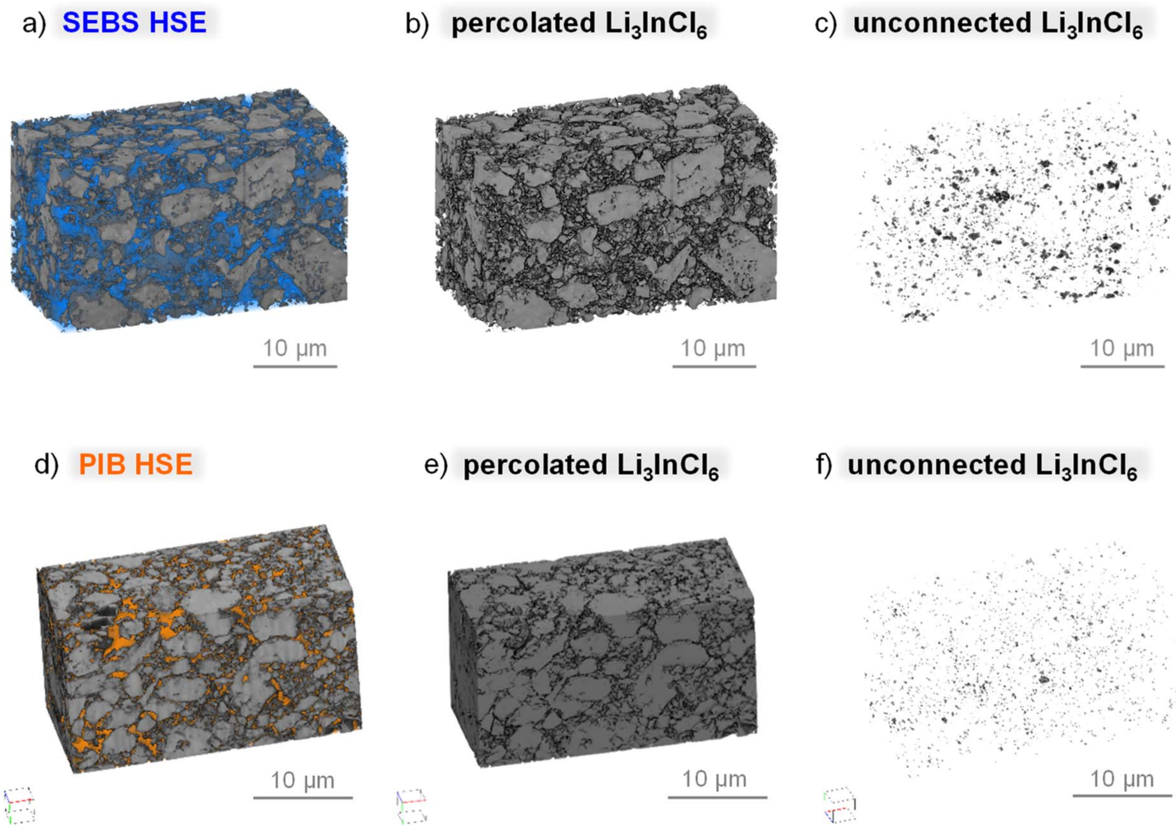

Fig. 7 3D reconstruction of (a) and (d) as SEBS HSE and PIB HSE with Li_3InCl_6 in grey and polymer in color (blue for SEBS and orange for PIB), (b) and (e) as percolated Li_3InCl_6 inorganic grains, and (c) and (f) as unconnected Li_3InCl_6 grains for SEBS HSE and PIB HSE, respectively.

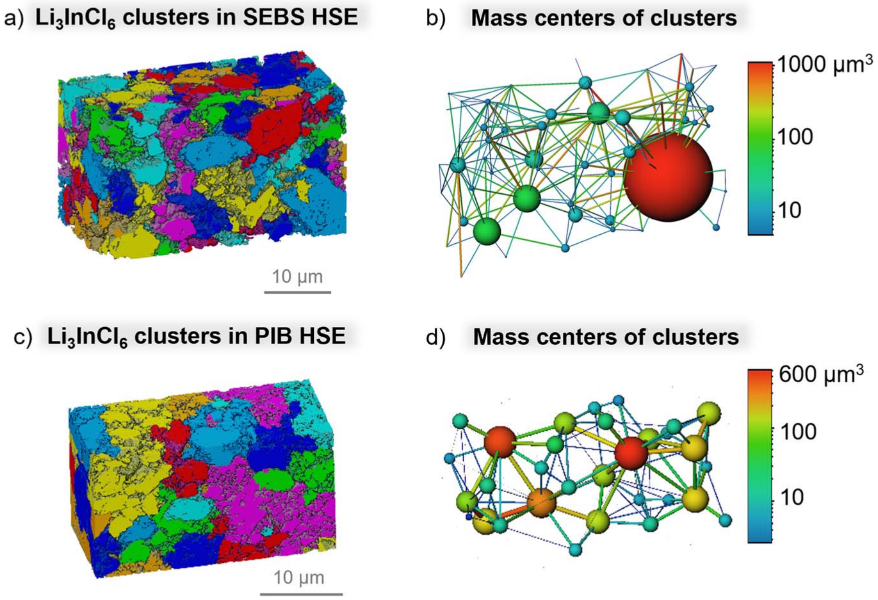

Fig. 8 Separated clusters of inorganic material (Li_3InCl_6) from cryo-plasma FIB-SEM images for (a) SEBS HSE and (c) PIB HSE, and connected mass centers of clusters for (b) SEBS HSE and (d) PIB HSE with corresponding color gradient scales.

tendency towards a terminal viscoelastic zone typical of homogeneous melts, where $G' \sim \omega^2$ and $G'' \sim \omega$. However, SEBS shows a predominantly elastic response ($G' > G''$) with a dependence of $G' \sim \omega^{0.35}$ and $G'' \sim \omega^{0.6}$, a result consistent with the presence of ordered microstructures as reported by Kossuth *et al.* for block copolymers. These authors reported $G' \sim \omega^{0.3}$ and $G' \sim \omega^{0.5}$ for systems with hexagonal and lamellar phases, respectively, and G' independent of frequency for the cubic arrangement. The observed power-law frequency dependence of 0.35 is very similar to the reported value for hexagonal phase systems. This change in properties can also be followed by a change in the phase angle (δ) (right side *y*-axes in Fig. 9a and b), with 0° for a fully elastic material to 90° for a fully viscous material. The clear bump (*i.e.*, the presence of a low frequency δ maximum), not exceeding 45°, visible for SEBS at 0.1 rad s^{-1} corresponds to the relaxation of microdomains (Fig. 9a), while

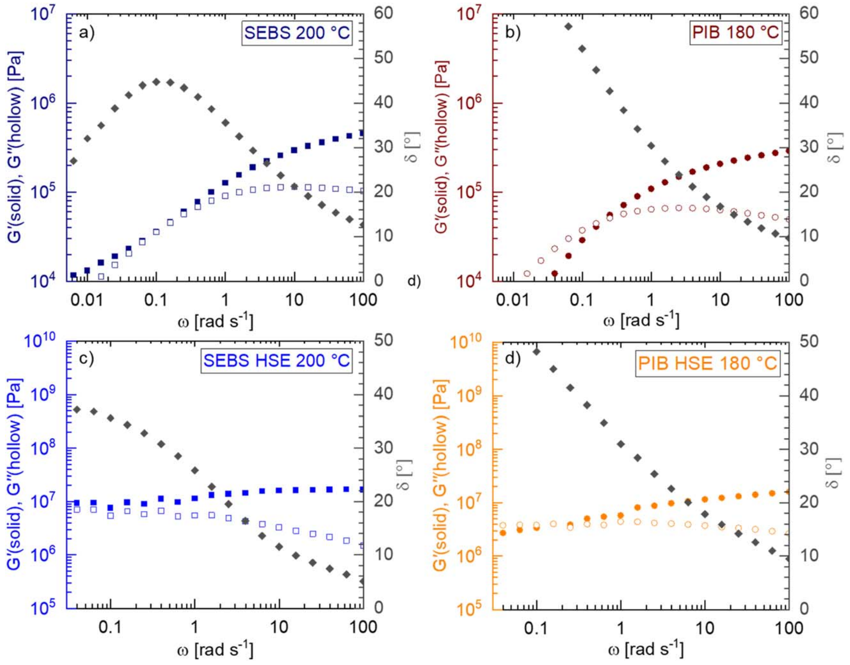

Fig. 9 G' and G'' moduli (left axis) and δ (right axis) as a function of angular frequency for (a) SEBS at 200 °C, (b) PIB at 180 °C, (c) SEBS HSE at 200 °C and (d) PIB HSE at 180 °C.

the continuous increase of δ up to 90° for PIB corresponds to the lack of any ordered structure of the homopolymer.[25] It is important to mention that block copolymers, which melt at $T < T_{ODT}$ (like SEBS, which melts at 200 °C but its T_{ODT} is at temperatures higher than 300 °C),[26] double constraint to motion suffers from midblock flexible chains owing to (a) chain entanglements (provided that the molecular weight of the midblock polymer is higher than its entanglement molecular weight) and (b) chain bridging between end blocks, leading to interconnected microdomains. However, in the disordered state ($T > T_{ODT}$), ordered microdomains disappear and chains are free to move: then $\delta \rightarrow 90°$ at low frequencies and the spectrum resembles that of homopolymers, reaching the terminal flow zone without secondary relaxations. Therefore, the selected temperature during the processing step for HSE, which is comprised of block copolymers, will be a key parameter.

In Fig. 9c and d, the small amplitude oscillatory shear sweeps for SEBS HSE and PIB HSE at their processing temperatures (200 °C and 180 °C, respectively) are plotted. The storage (G') and loss (G'') moduli are higher for HSEs than for neat polymers due to the presence of the inorganic material; however, the trend is similar to that of neat polymers. SEBS HSE exhibits storage and loss moduli of 1.6×10^8 Pa and 3.1×10^7 Pa at 10 rad s^{-1}, respectively, with a 552 and 282 times increase in the corresponding moduli when compared to neat SEBS. In contrast, PIB HSE exhibits storage and loss moduli of 1.2×10^7 Pa and 3.6×10^6 Pa at 10 rad s^{-1}, respectively, with a 57 and 60 times increase in the corresponding moduli compared to the neat PIB. The storage modulus increase in PIB HSE is about 9.7 times less when compared to the G' change in SEBS HSE. Moreover, similarly to neat polymers, no crossing point for G' and G'' values was observed for SEBS HSE, unlike PIB HSE at 0.1 rad s^{-1}. In the case of HSEs, the low-frequency region is limited to approximately 0.03 rad s^{-1}. The hybrid structures are highly sensitive to deformation; thus, a low amplitude was applied to preserve the linear viscoelastic conditions, which reduced the signal at lower frequencies. Despite this, it is still possible to identify the polymer relaxation patterns of the neat polymers in the hybrid systems. Similarly to Fig. 9a, the clear bump in phase angle that does not exceed 45° is observed for SEBS HSE at 0.1 rad s^{-1} related to the microdomain relaxation of the SEBS polymer binder (Fig. 9c), whereas the continuously increasing delta value recorded for PIB HSE (Fig. 9d) corresponds to the relaxation of the polymeric chain undisturbed by any structure of the material as seen for neat PIB (Fig. 9b). These results indicate that the SEBS chain mobility in SEBS HSE requires relaxation times larger than the PIB chain mobility in PIB HSE due to blocking effect of the ordered morphology. Therefore, at the same pressure and time of the processing step, SEBS in SEBS HSE requires more time to accommodate its structure, and in turn, to percolate inorganic electrolyte particles in contrast to PIB in PIB HSE, which flows due to its disordered morphology, allowing to achieve more connected LIC particles. Consequently, the rheological results support the conductivity, lithium diffusion and structural results of the hybrids and confirm the crucial impact of the non-conducting polymer structure (ordered or disordered) on the transport properties of HSEs.

Finally, the limiting current density of HSEs was evaluated by conducting lithium plating and stripping tests in a lithium symmetric cell configuration to investigate the impact of the polymer morphology on the electrochemical performance of HSEs. As the electrolytes investigated in this work are LIC-based, it is well known that they require the application of an interlayer to avoid side reactions with Li metal.[27,28] The Li_6PS_5Cl (LPSCl) sulfide electrolyte was chosen as the protecting layer because it has already been reported as an interlayer enabling the electrochemical characterization of Li_3InCl_6 with Li metal.[29,30] First, the galvanostatic cycling of a lithium symmetrical cell with a LPSCl pellet at different current densities (25, 50, 100, 200, 400, 800 and 1000 μA cm^{-2}) at 25 °C was performed to evaluate the critical current density of the inorganic interlayer for further applications with HSEs. The detailed preparation of the setup used for these measurements is explained in the Experimental part. The results are presented in Fig. 10a with the corresponding cell configuration schemes. LPSCl exhibits a stable potential from 25 μA cm^{-2} to 400 μA cm^{-2}; however, a voltage drop indicating dendrites or short-circuit is observed from 800 μA cm^{-2} to 1000 μA cm^{2}, demonstrating the stability of the argyrodite interlayer up to 400 μA cm^{-2}.

Furthermore, the LPSCl interlayer was applied on both sides of the HSEs in the Li-symmetric cells to investigate the limiting current density for each of our hybrids using the same protocol with different current densities as for the Li|LPSCl|Li cell. The results of lithium plating and stripping at RT and 10 MPa, along with the corresponding cell configurations, are presented in Fig. 10b and c for SEBS HSE and PIB HSE, respectively. The cell potential of the SEBS HSE remained stable (around 35 mV) at 25 μA cm^{-2} and exhibited voltage instability after applying 50 μA cm^{-2}. The potential values vary significantly with a further increase in current density until 1000 μA cm^{-2}. The unstable voltage curve and increased overpotential during the Li stripping/plating test indicate a significant ohmic resistance in the SEBS HSE cell, which is likely correlated to the sluggish Li$^+$ transport within the SEBS, based on the previous discussion. However, lithium plating and stripping measurements for cells with PIB HSE presented a stable potential for each current density, from 28 mV to 420 mV for 25 μA cm^{-2} to 400 μA cm^{-2}, respectively, which is consistent with the critical current density also observed for LPSCl, although achieving higher overpotential values when compared to SEBS HSE (up to 160 mV at 400 μA cm^{-2}). The cell with PIB HSE exhibited notable potential variations at 800 μA cm^{-2} and, even more, at 1000 μA cm^{-2}. These results are in line with our previous observations from ionic transport investigations, 3D reconstructions and rheology measurements for the HSEs. The hybrid based on an ordered block copolymer (SEBS) features ionic pathways with increased tortuosity, and probably, the inorganic particles are not sufficiently connected to maintain the higher current density in contrast to the HSE based on the disordered polymer (PIB), which promotes ion conduction within the LIC network. To the best of our knowledge, these findings provide, for the first time, insight into the choice of non-conducting polymer binders based on their morphology and the design of the HSEs with improved Li-ion transport properties.

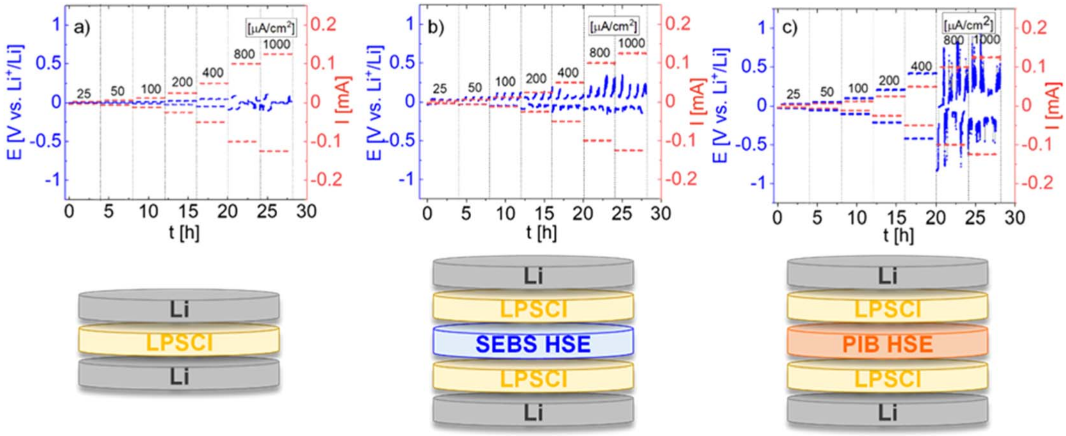

Fig. 10 Electrochemical performance of (a) LPSCl pellet and (b) LPSCl/SEBS HSE/LPSCl and (c) LPSCl/PIB HSE/LPSCl Li symmetric cells under different current densities ranging from 25 to 1000 μA cm^{-2} at RT and 10 MPa, with the corresponding configurations shown below.

Conclusions

In summary, we have investigated the effect of polymer morphology on transport properties, comparing an ordered nanostructured block copolymer SEBS and a disordered homopolymer PIB in inorganic-rich hybrid solid electrolytes (HSEs) based on a halide electrolyte (Li_3InCl_6). After electrolyte processing, no pressure effect was observed on the ionic conductivity of the flexible electrolyte membranes (~30 μm), which is beneficial for implementation in ASSB manufacturing lines. The ionic transport was more thermally activated for PIB HSE (0.24 eV) than for SEBS HSE (0.17 eV), reaching ionic conductivities of 0.39×10^{-4} S cm^{-1} and 0.23×10^{-4} S cm^{-1} at 30 °C, for PIB HSE and SEBS HSE, respectively. Moreover, PIB HSE presented improved cycling performance and a higher critical current density (CCD) (400 μA cm^{-2}) than SEBS HSE (25 μA cm^{-2}). Cryo-plasma FIB-SEM images and rheology results indicate that the disordered elastomer polymer binders lead to more connected LIC particles, and therefore, promote more ion-conducting channels in the inorganic LIC electrolyte compared to the nanostructured ones. Moreover, rheology results indicate that HSEs composed of non-conducting block copolymers should be processed in the disordered state ($T > T_{ODT}$), in which ordered microdomains disappear and chains are free to move, reaching the terminal flow zone. Consequently, the processing temperature of HSE is a key parameter to get optimized HSEs. We believe that our results shed new light on the choice and design of non-polar polymer structures for obtaining hybrid electrolytes with improved ionic transport properties for battery application.

Data availability

Data supporting the findings of this study are available within the article.

Conflicts of interest

The authors declare no financial interest.

Acknowledgements

The authors acknowledge the financial support from the Spanish Ministry of Science, Agencia Estatatal de Investigacion (PID2020-115080RA-I00, CNS2023-144408). The Basque Government, Department of Education through PIBA_2024_1_0051 is acknowledged. We acknowledge the support from the María de Maeztu Excellence Unit CEX2023-001303-M funded by MCIN/AEI/10.13039/501100011033. The authors would also like to thank Cameron A. Gurwell from Professor Goward's group for his assistance in sample preparations and pressure calibrations of the home-made cell for PFG measurements. L. F. acknowledges financial support from the German Academic Scholarship Foundation. A. A. and A. I. acknowledge the Grant PID2021-123438NB-I00 funded by MCIN/AEI/10.13039/501100011033 and by "ERDF A way of making Europe" and financial support from Eusko Jaurlaritza, code: IT1566-22. We acknowledge "Maria de Maeztu" Units of Excellent Programme No. CEX2020-001038-M and project EQC2021-007107-P of "Subprograma Estatal de Infraestructuras de Investigación y Equipamiento Científico-Técnico" of Spanish Ministry of Science and Innovation. We also acknowledge the support of the Slovak Research and Development Agency (APVV-20-0111). We acknowledge the financial support of the Basque Government through the IKUR Strategy. This work has received financial support from the European Union's Horizon Europe research and innovation programme under grant agreement no. 101069726 (SEATBELT project). Views and opinions expressed are, however, those of the author(s) only and do not necessarily reflect those of the European Union or CINEA. Neither the European Union nor the granting authority can be held responsible for them. Finally, we gratefully acknowledge the ALBA synchrotron facility (Proposal number 2024098628) for the funding and help to perform the WAXS experiments at BL11-NCD-SWEET beamline with the collaboration of ALBA staff.

References

1 T. Yu, X. Yang, R. Yang, X. Bai, G. Xu, S. Zhao, Y. Duan, Y. Wu and J. Wang, Progress and Perspectives on Typical Inorganic

Solid-State Electrolytes, *J. Alloys Compd.*, 2021, **885**, 161013, DOI: **10.1016/j.jallcom.2021.161013**.

2 M. R. Bin Mamtaz, X. Michaud, H. Jo and S. S. Park, Stress and Manufacturability in Solid-State Lithium-Ion Batteries, *Int. J. Precis.*, 2023, **10**, 1093–1137, DOI: **10.1007/s40684-023-00519-2**.

3 P. Mirmira, C. Fuschi, Z. Umlauf, P. Ma, E. S. Doyle, M. C. Vu and C. V. Amanchukwu, Impact of Processing Methodology on the Performance of Hybrid Sulfide-Polymer Solid State Electrolytes for Lithium Metal Batteries, *J. Electrochem. Soc.*, 2024, **171**(3), 030508, DOI: **10.1149/1945-7111/ad2d3e**.

4 T. T. Vu, H. J. Cheon, S. Y. Shin, G. Jeong, E. Wi and M. Chang, Hybrid Electrolytes for Solid-State Lithium Batteries: Challenges, Progress, and Prospects, *Energy Storage Mater.*, 2023, **61**, 102876, DOI: **10.1016/j.ensm.2023.102876**.

5 X. Li, J. Liang, N. Chen, J. Luo, K. R. Adair, C. Wang, M. N. Banis, T. Sham, L. Zhang, S. Zhao, S. Lu, H. Huang, R. Li and X. Sun, Water-Mediated Synthesis of a Superionic Halide Solid Electrolyte, *Angew. Chem.*, 2019, **131**(46), 16579–16584, DOI: **10.1002/anie.201909805**.

6 X. Li, J. Liang, J. Luo, M. Norouzi Banis, C. Wang, W. Li, S. Deng, C. Yu, F. Zhao, Y. Hu, T. K. Sham, L. Zhang, S. Zhao, S. Lu, H. Huang, R. Li, K. R. Adair and X. Sun, Air-Stable Li3InCl6 Electrolyte with High Voltage Compatibility for All-Solid-State Batteries, *Energy Environ. Sci.*, 2019, **12**(9), 2665–2671, DOI: **10.1039/c9ee02311a**.

7 I. D. Seymour, E. Quérel, R. H. Brugge, F. M. Pesci and A. Aguadero, Understanding and Engineering Interfacial Adhesion in Solid-State Batteries with Metallic Anodes, *ChemSusChem*, 2023, **16**(12), 202202215, DOI: **10.1002/cssc.202202215**.

8 S. Sen, E. Trevisanello, E. Niemöller, B. X. Shi, F. J. Simon and F. H. Richter, The Role of Polymers in Lithium Solid-State Batteries with Inorganic Solid Electrolytes, *J. Mater. Chem. A*, 2021, **9**(35), 18701–18732, DOI: **10.1039/d1ta02796d**.

9 P. Mirmira, C. Fuschi, W. Gillett, P. Ma, J. Zheng, Z. D. Hood and C. V. Amanchukwu, Nonconductive Polymers Enable Higher Ionic Conductivities and Suppress Reactivity in Hybrid Sulfide-Polymer Solid State Electrolytes, *ACS Appl. Energy Mater.*, 2022, **5**(7), 8900–8912, DOI: **10.1021/acsaem.2c01388**.

10 C. Wang, C. Wang, M. Li, S. Zhang, C. Zhang, S. Chou, J. Mao and Z. Guo, Design of Thin Solid-State Electrolyte Films for Safe and Energy-Dense Batteries, *Mater. Today*, 2024, **72**, 235–254, DOI: **10.1016/j.mattod.2023.11.016**.

11 S. Montes, A. Beutl, A. Paolella, M. Jahn and A. Tron, Cost-Effective Solutions for Lithium-Ion Battery Manufacturing: Comparative Analysis of Olefine and Rubber-Based Alternative Binders for High-Energy Ni-Rich NCM Cathodes, *ChemElectroChem*, 2024, 202400465, DOI: **10.1002/celc.202400465**.

12 K. Lee, S. Kim, J. Park, S. H. Park, A. Coskun, D. S. Jung, W. Cho and J. W. Choi, Selection of Binder and Solvent for Solution-Processed All-Solid-State Battery, *J. Electrochem. Soc.*, 2017, **164**(9), A2075–A2081, DOI: **10.1149/2.1341709jes**.

13 D. H. S. Tan, A. Banerjee, Z. Deng, E. A. Wu, H. Nguyen, J. M. Doux, X. Wang, J. H. Cheng, S. P. Ong, Y. S. Meng and Z. Chen, Enabling Thin and Flexible Solid-State Composite Electrolytes by the Scalable Solution Process, *ACS Appl. Energy Mater.*, 2019, **2**(9), 6542–6550, DOI: **10.1021/acsaem.9b01111**.

14 A. Tron, R. Hamid, N. Zhang, A. Paolella, P. Wulfert-Holzmann, V. Kolotygin, P. López-Aranguren and A. Beutl, Film Processing of Li6PS5Cl Electrolyte Using Different Binders and Their Combinations, *J. Energy Storage*, 2023, **66**, 107480, DOI: **10.1016/j.est.2023.107480**.

15 N. Stankiewicz, M. Criado-Gonzalez, J. L. Olmedo-Martínez, E. Matxinandiarena, P. López-Aranguren, F. Bonilla, G. Accardo, D. Saurel, D. Devaux and I. Villaluenga, In Situ Hybrid Solid-State Electrolytes for Lithium Battery Applications, *ACS Appl. Polym. Mater.*, 2024, **6**, 14124–14132, DOI: **10.1021/acsapm.4c00473**.

16 N. S. Karode, A. Poudel, L. Fitzhenry, S. Matthews, P. R. Walsh and A. B. Coffey, Evaluation of Interfacial Region of Microphase-Separated SEBS Using Modulated Differential Scanning Calorimetry and Dynamic Mechanical Thermal Analysis, *Polym. Test.*, 2017, **62**, 268–277, DOI: **10.1016/j.polymertesting.2017.07.006**.

17 M. A. Paglicawan and J. R. Celorico, Properties of Styrene-Ethylene-Butylene Styrene Block Copolymer/Exfoliated Graphite Nanoplatelets Nanocomposites, *Polym. Polym. Compos.*, 2021, **29**(9), S154–S165, DOI: **10.1177/0967391121991290**.

18 C. Peinado, T. Corrales, M. J. García-Casas, F. Catalina, V. R. S. Quiteria and M. D. Parellada, Chemiluminescence from Poly(Styrene-b-Ethylene-Co-Butylene-b-Styrene) (SEBS) Block Copolymers, *Polym. Degrad. Stab.*, 2006, **91**(4), 862–874, DOI: **10.1016/j.polymdegradstab.2005.06.020**.

19 P. T. Callaghan, *Principles of Nuclear Magnetic Resonance Microscopy*, 1991, pp. 57–63.

20 W. S. Price, Pulsed-field gradient nuclear magnetic resonance as a tool for studying translational diffusion: Part 1. Basic theory, *Concepts Magn. Reson.*, 1997, **9**, 299–336, DOI: **10.1002/(SICI)1099-0534(1997)9:5<299::AID-CMR2>3.0.CO;2-U**.

21 B. Hennequart, M. Platonova, R. Chometon, T. Marchandier, A. Benedetto, E. Quemin, R. Dugas, C. Lethien and J. M. Tarascon, Atmospheric-Pressure Operation of All-Solid-State Batteries Enabled by Halide Solid Electrolyte, *ACS Energy Lett.*, 2024, 454–460, DOI: **10.1021/acsenergylett.3c02513**.

22 S. Duan, M. Cattaruzza, V. Tu, R. M. Auenhammer, R. Jänicke, M. K. G. Johansson, F. Liu and L. E. Asp, Three-Dimensional Reconstruction and Computational Analysis of a Structural Battery Composite Electrolyte, *Commun. Mater.*, 2023, **4**(1), 1–9, DOI: **10.1038/s43246-023-00377-0**.

23 G. Neusser, S. Eppler, J. Bowen, C. J. Allender, P. Walther, B. Mizaikoff and C. Kranz, FIB and MIP: Understanding Nanoscale Porosity in Molecularly Imprinted Polymers: Via 3D FIB/SEM Tomography, *Nanoscale*, 2017, **9**(38), 14327–14334, DOI: **10.1039/c7nr05725c**.

24 D. Hlushkou, A. E. Reising, N. Kaiser, S. Spannenberger, S. Schlabach, Y. Kato, B. Roling and U. Tallarek, The Influence of Void Space on Ion Transport in a Composite Cathode for All-Solid-State Batteries, *J. Power Sources*, 2018, **396**, 363–370, DOI: 10.1016/j.jpowsour.2018.06.041.

25 M. B. Kossuth, D. C. Morse and F. S. Bates, Viscoelastic Behavior of Cubic Phases in Block Copolymer Melts, *J. Rheol.*, 1999, **43**(1), 167–196, DOI: 10.1122/1.550981.

26 A. Arevalillo, M. E. Muñoz, A. Santamaría, L. Fraga and J. A. Barrio, Novel Rheological Features of Molten SEBS Copolymers: Mechanical Relaxation at Low Frequencies and Flow Split, *Eur. Polym. J.*, 2008, **44**(10), 3213–3221, DOI: 10.1016/j.eurpolymj.2008.07.028.

27 L. M. Riegger, R. Schlem, J. Sann, W. G. Zeier and J. Janek, Lithium-Metal Anode Instability of the Superionic Halide Solid Electrolytes and the Implications for Solid-State Batteries, *Angew. Chem.*, 2021, **133**(12), 6792–6797, DOI: 10.1002/ange.202015238.

28 K. Kim, D. Park, H. G. Jung, K. Y. Chung, J. H. Shim, B. C. Wood and S. Yu, Material Design Strategy for Halide Solid Electrolytes Li3MX6(X = Cl, Br, and I) for All-Solid-State High-Voltage Li-Ion Batteries, *Chem. Mater.*, 2021, **33**(10), 3669–3677, DOI: 10.1021/acs.chemmater.1c00555.

29 Y. Kim, C. Juarez-Yescas, D. W. Liao, M. K. Jangid, P. Joshi, H. Yang, B. Zahiri, P. V. Braun and N. P. Dasgupta, Thin Free-Standing Sulfide/Halide Bilayer Electrolytes for Solid-State Batteries Using Slurry Processing and Lamination, *ACS Energy Lett.*, 2024, **9**(4), 1353–1360, DOI: 10.1021/acsenergylett.4c00092.

30 T. Ma, Z. Wang, D. Wu, P. Lu, X. Zhu, M. Yang, J. Peng, L. Chen, H. Li and F. Wu, High-Areal-Capacity and Long-Cycle-Life All-Solid-State Battery Enabled by Freeze Drying Technology, *Energy Environ. Sci.*, 2023, 2142–2152, DOI: 10.1039/d3ee00420a.